An All-Polarization, Beamforming, and DoA Ready, Γ–Dipole Antenna Array

Dimitrios G. Arnaoutoglou, Antigone-Aikaterini G. Kyriakou, Theodoros N. F. Kaifas, *Senior Member, IEEE*, Georgios Ch. Sirakoulis, *Senior Member, IEEE*, and George A. Kyriacou, *Senior Member, IEEE*

Abstract— A novel miniature all-polarization Γ antenna array for demanding 5G and the Internet of Things (IoT) applications is proposed. The antenna is designed to be able to perform direction of arrival (DoA) and beamforming keeping the antenna's footprint as minimal as possible to fit in or wrapped around any IoT device. It is a nonuniform square array comprised of novel right-corner dipoles which are mirror-placed to additionally allow all polarization properties. These properties are inherited from its approximate equivalence to a cross-dipole antenna with additional features and flexibility. An analytical mathematical formulation is presented resulting in a closed form for the Γ–dipole as well as the four dipoles array. Numerical simulations proved the antenna performance and verified that all of its features are approximately retained even when it is curved. The antenna is prototyped in both an improvised wire dipole (planar or curved) and as printed on an FR-4 substrate. The measured results confirmed the analytical and numerical ones regarding the antenna all-polarization, beamforming, and DoA features.

Index Terms— All-polarization antenna, direction of arrival, (DoA) Internet of Things (IoT) antennas, miniature antennas.

I. INTRODUCTION

THERE are two general paths to the Internet of Things (IoT) antenna design, the general purpose, and the application-specific ones. In the first case, the antenna is required to exhibit characteristics that can comply with general operational, deployment, and service demands. Quasi-omnidirectional, nearly all polarization far-field with good enough matching and efficient operation on the frequency range of interest usually is enough for a general-purpose device [1], [2], [3]. In addition, some durability and yield on deformation, varying environment deployments, deposition, and construction tolerances may also be desirable. In the second case, the antenna is to exhibit wide, dual,

or multifrequency operation. May be employed on specific macro (indoor, outdoor, and satellite) and micro-environment (attached on a specific host). Also, it may be required to exhibit multibeam and multifunction characteristics while working under specific communication protocols. In this framework, there is a need for new, or re-engineered antennas, to be added in the antenna designer's suite. The purpose is to be able to both serve on a wider range of applications and at the same time to allow for fine-tuning to deliver high scores on key antenna performance indicators.

In the work at hand, we contribute an antenna design that, while can serve as a general-purpose device, at the same time, apart from isotropic and all-polarization response, can deliver beamforming and direction of arrival (DoA), functions. The rationale behind such a goal (general plus specific purpose device) can be traced on the certain facts (need for multiple beams, DoA awareness, and polarization agility) that feed the difficulty of the IoT antenna selection [4], [5], [6].

Indeed, currently, the IoT interconnected devices are communicating mainly using nearly isotropic antennas. In order to maintain the unceasing data transfer in an area, there is a need for new miniature antennas with high efficiency. It is imperative for the IoT operation that each device is aware of its neighboring ones, primarily their direction, and as a second priority, their distance. To serve this purpose, antennas exhibiting multiple partially overlapping directional radiation patterns-beams are desirable (beamforming). Transmitting and receiving through contiguous beams provides the information needed to estimate the IoT-source direction, namely, offering DoA functionality. Besides the DoA function, the IoTs equipped with directional beams may exploit them toward more efficient communication. Apart from directional beams, the antenna should also offer an isotropic radiation pattern, since it is highly probable that this pattern would be utilized in the initialization or handshaking process.

Furthermore, the radiated beams may exhibit a [intentionally—line of sight (LOS) or unintentionally—non-line of sight (NLOS)], specific polarization, linear polarization (LP), such as horizontal, vertical, or even axial, or elliptical or circular polarization (CP). Besides that, the IoT devices are expected to be arbitrarily placed and oriented by nontrained individuals and hence specific polarization alignment will be impossible to be ensured. Thus, an antenna capable of receiving any kind of polarization is essential in places where the communication link is not established

with LOS and the receiving signal has a random polarization caused by the reflections and scattering. Thus, a competent antenna should include in its repertoire, preferably, all polarization, multibeam modes of operation. A particular application that can benefit from such an "all-polarization" antenna refers to the smart house, especially regarding the IoT facilities supporting elderly people [7], [8].

A vast variety of antennas have been proposed in the literature to fulfill the aforementioned need for all-polarization antenna for the IoT or RFID applications [6], [9], [10]. Different all-polarization antennas have been proposed in the literature such as tri-orthogonal [11], [12], MIMO cubes [13], [14], [15], [16], [17], and dielectric resonators [18]. The tri-orthogonal antennas exhibit high robustness when transmitter–receiver antennas are presented with misalignment. Furthermore, an increased capacity performance is displayed in collocated antennas in a tri-orthogonal alignment [13], [19], [20], [21]. However, they are bulky structures with increased volume making it impractical for compact IoT devices. The cross dipoles are the most popular antenna generating dual-polarized and circular polarized radiation maintaining a low profile keeping the power efficiency at high levels [22]. In addition, an all-polarization antenna is also useful for RF energy harvesting applications providing received RF signal regardless of polarization [23], [24], [25]. Going through the crossed dipole literature, a question or an idea may arise as, "is it possible to retain the same antenna properties when the half dipole or a corner dipole is employed."

The innovation of this work is clearly outlined by the succeed answer. In this article, it is proved that indeed a corner Γ–dipole preserves all of the polarization-related crossed dipole properties while reducing its profile to one-quarter size. Especially, properly rotated corner Γ–dipoles form a 2 × 2 square array with a profile equal to a single-size crossed-dipole that inherits the polarization agility. Note that, this array is not a uniform one since the elements are rotationally different. Nevertheless, the educated choices on the position and rotation of the Γ–dipoles equip the proposed device with diverse beamforming potential. Indeed, near the broadside (normal to the array's surface) with proper phasing, the array behaves like a uniform planar array (UPA) allowing for the relative conventional beamforming approach to be employed. On the other hand, near the endfire (parallel to the array surface), the array changes its behavior to a uniform circular array (UCA), allowing for the relative implications in beamforming. Furthermore, what is impressive is that this array may be curved or even distorted, so as to be wrapped on the package of the IoT-served device while retaining the desired antenna array properties at a very high degree. Thus summarizing, with the appropriate phasing this array may support any polarization and to shape its radiation pattern from almost isotropic to a directive one offering even DoA awareness in a 3-D space, which is tested and verified.

The article is organized as follows. In Section II, the antenna development rationale is presented. The antenna's mathematical analysis is given in Section III, while the antenna fabrication and characterization details are provided in Section IV. Various aspects of the antenna's performance,

like polarization, beamforming, DoA agility, and also deformation resilience are presented in detail providing mathematical results, simulation, and measurements data in Section V.

II. Gamma, Γ, Dipole and Antenna Array

The proposed antenna array is contributed to the current section. The goal of the study is to present a simple and inexpensive radiator capable of delivering an:

1) all polarization property and
2) a number of beams to achieve nearly semi-spherical coverage.

In addition, general requirements for the IoT antennas should apply. ISM, at maybe 2.4 GHz, operation with a small footprint, resilient performance at a broad range of indoor/outdoor applications and relative insensitive and undegraded response to radiator deformation, nearby scattering objects, and also construction tolerances.

Let us consider a plane wave incident on an antenna with an equivalent radiation vector $\vec{h}$. It is well known that the induced open circuit voltage at the antenna's terminals reads

$$V_{OC} = \vec{h} \cdot \vec{E}^i. \tag{1}$$

In case the antenna exhibits a small footprint (like the one we need to develop), then, loosely but intuitively thinking, at reception the $\vec{h}$ vector should match the mean equivalent current density on the antenna. Again, due to the small footprint, this current density should be more or less constant and thus should match the antenna free-current conducting path, meaning the antenna conductor. With those thoughts in mind (following a somehow reverse engineering approach), the antenna development path is presented in Table I.

We should add, here, some comments related to the antenna novelty. First of all, our Γ–dipole antenna is a particular case of the well-known V-antenna (usually complement of the rhombic antenna) [26]. However, as such the V-antenna is not fixed to a 90° angle and more importantly is essentially established as a traveling wave antenna and not a resonant one, like the Γ–dipole is. Having said that, the solid contribution is based on the alternative way that the #2 and #4 element Γ–dipole array antenna is formed. Indeed, conventional antenna array formation dictates that, usually, one type of element is cloned and arranged by following some regular 1-D or 2-D grid. Here, the elements are the same but for the array, rotated clones of them are used. This may complicate the relative analysis, since the classical pattern multiplication approach does not apply, but opens a broad realm of antenna response capabilities. The proposed antenna is extremely easy and inexpensive in construction, but also extremely durable in its response, exhibiting, oddly enough, at the same time a broad range of multifunction potential.
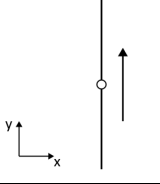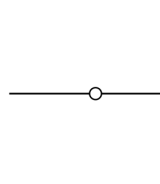
Those findings are to be provided with a solid mathematical–theoretical analysis in Section III and elaborated in detail, by simulation and measurements data, in the rest of this article.

III. Theoretical Analysis

In this section, the mathematical analysis is derived for each corner dipole and for the 2 × 2 array in order to assess

TABLE I
Γ–DIPOLE ANTENNA AND ARRAY DEVELOPMENT CONCEPT

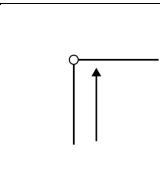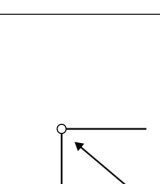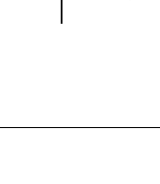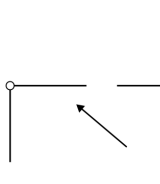| Antenna Configuration	Antenna's Open Circuit Voltage
	For the classical $\lambda/2$ dipole the open circuit voltage at the antenna's terminals follows the well-known formula (1)).
	When the incident field is polarized normal to the antenna's radiation vector the open circuit voltage is zero.
	The detection of every polarization of electromagnetic wave is achieved by bending the dipole to look like the Greek capital letter 'Gamma' where the two branches are being orthogonal to each other $V_{OC} = \vec{h}_x \cdot \vec{E}^i + \vec{h}_y \cdot \vec{E}^i = \vec{h}_y \cdot \vec{E}^i$
	Even for the Γ-dipole, there are angles, $\phi = 3\pi/4$, $7\pi/4$, of the polarization of the incident field that force the antenna to provide zero open circuit voltage. $V_{OC} = \vec{h} \cdot \vec{E}^i = (\hat{x} + \hat{y}) \cdot ((-\hat{x} + \hat{y})) = (-1 + 1) = 0$. This phenomenon is due to the position of the two branches of the dipole in such way that when the incoming electromagnetic field is incident with polarization angles $\phi = 3\pi/4$ or $7\pi/4$, the induced surface currents on the two arms flow in opposite directions leading to zero induced voltage.
	1D Array: All polarization, quasi-isotropic pattern and scan in zx plane. The solution to this problem is to include a second Γ-dipole rotated by $-90°$, with respect to the first. Note that, the second element is a mirror image of the first with respect to zy plane to minimize inter-element coupling. The second Γ-dipole displays a maximum when the first displays a zero, (previous case). Thus, the radiation pattern becomes quasi - omnidirectional, enabling the transmission, (reception), of a signal to, (from), every azimuth angle. Combining the two voltages we achieve an all-polarization detection using only two elements.
	2D array: All polarization, quasi-omni pattern and scan both on zx and zy planes. In the previous configuration a scan on zx plane is achieved. By using a second two element array mirrored on the zx plane, a scan capability in the zy plane is also enabled. Namely, enabling both azimuth and elevation beam scanning or beam pointing in 3D. The Γ-dipoles are placed in the corners of a square to minimize the cross coupling between them.

the radiation pattern of the structure. For the formulation, the dipoles are assumed to be very thin cylinders or strips (ideally filamentary, zero diameter) placed in free space (neglecting the effect of the substrate).

A. Γ–Dipole Current Distribution

The proposed antenna is a resonant one and thus a standing wave current distribution is quite an adequate assumption.
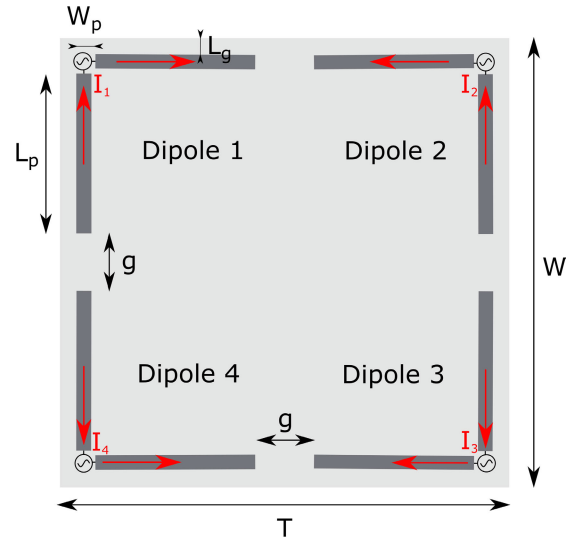

Fig. 1. Top view of the proposed antenna and its corresponding dimensions as modeled in the proposed work. The direction of the current flow is indicated with red arrows. The dielectric constant of the substrate is $\epsilon_r = 4$.

Indeed, the current distribution of the dipole #1 of Fig. 1 can be approximated by sinusoidal distribution similar to ordinary dipoles as in [27]. A voltage source feed is placed in the gap between the two corner arms.

$$\vec{I}_e(x', y', z') = \begin{cases} \hat{\mathbf{x}} I_0 sin\left[k\left(\dfrac{l}{2} - x'\right)\right], & 0 \le x' \le \dfrac{l}{2} \\ \hat{\mathbf{y}} I_0 sin\left[k\left(\dfrac{l}{2} + y'\right)\right], & -\dfrac{l}{2} \le y' \le 0 \end{cases} \quad (2)$$

where I_0 is the excited current amplitude k is the free space wavenumber and l is the total length of the Γ–dipole. Formula (2) assumes that the antenna is center-fed and the current vanishes at the end points ($x' = (l/2)$, $y' = 0$) and ($x' = 0$, $y' = -(l/2)$), as depicted Fig. 2(a). Equation (2) was verified using characteristic mode analysis (CMA). The current distribution of the dipole #1 of Fig. 1 can be approximated by sinusoidal distribution similar to ordinary dipoles as in Balanis [27], taking care to consider the current flowing as in Fig. 3 (red arrows) to maximize the radiation by a voltage source feed placed in the gap between the two corner branches. Particularly, assuming a cylindrical corner dipole with a small diameter, e.g., 0.1 mm, a total of length $\lambda/2 = 60$ mm (resonating at 2.45 GHz), it was simulated utilizing the integral equation solver of CST [28] to extract the CMA. The eigen-current of the first/dominant mode is displayed in Fig. 3. The CMA eigen-analysis is in agreement with the assumed distribution (2), as it is shown in Fig. 2(a).

B. Γ–Dipole Far-Field

In this section, the closed-form far-field response based on standing wave current distribution on the Γ–dipole antenna is given.

1) Closed Form Far-Field of the Γ–Dipole: Following the same procedure as Balanis [27] and Orfanidis [29], the magnetic potential ($\vec{A}$) is derived for the current distribution of (2) and the notation depicted in Fig. 2

$$\mathbf{A}(x, y, z) = \frac{\mu}{4\pi} \int_C \vec{I}_e(x', y', z') \frac{e^{-jkR}}{R} dl. \quad (3)$$
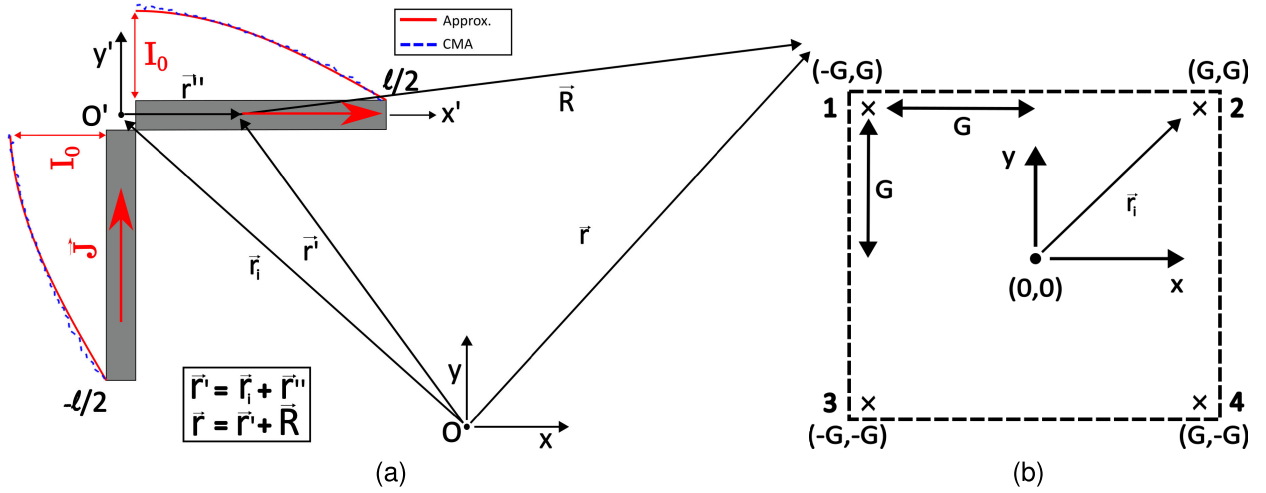
Fig. 2. (a) Current distribution in the case of the Γ–dipole #1 as approximate in (2) and validated exploiting CMA. The depicted notation is utilized for the analytical field evaluation, for the field $r, R \to \infty$ and $\vec{r}//\vec{R}$. (b) Array configuration, dipoles' centers at $\vec{r}_i = x_i\hat{x} + y_i\hat{y}$ where $(x_i, y_i) = (-G, G), (G, G), (G, -G)$, and $(-G, -G)$.
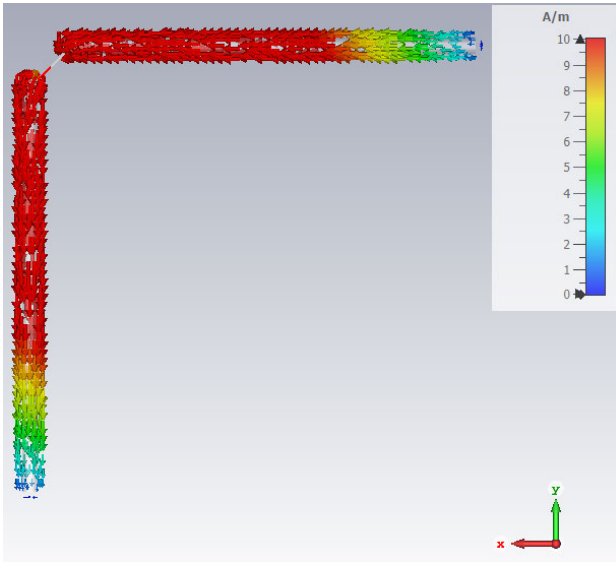

Fig. 3. First dominant surface eigen-current mode extracted from CMA corner Γ–dipole's #1 with length $\lambda/2 = 60$ mm to resonate at 2.45 GHz.

For the far-field approximation $(\vec{R}//\vec{r})$ (3) reads

$$A_x = I_0 \frac{\mu e^{-jkr}}{4\pi r} \int_0^{l/2} sin\left[k\left(\frac{l}{2} - x'\right)\right]e^{jk_x x'}dx' \quad (4)$$

$$A_y = I_0 \frac{\mu e^{-jkr}}{4\pi r} \int_{-l/2}^0 sin\left[k\left(\frac{l}{2} + y'\right)\right]e^{jk_y y'}dy' \quad (5)$$

where $\vec{k} \cdot \vec{r}' = k_x x' + k_y y' + k_z z'$ and $k_x = ksin(\theta)cos(\phi)$, $k_y = ksin(\theta)sin(\phi)$.

The next step involves the integration of the terms of (4) and (5) based on [27]. The resulted values of $\mathbf{A}_x$ and $\mathbf{A}_y$ are evaluated as

$$A_x = I_0 \frac{\mu e^{-jkr}}{4\pi r} \frac{ke^{jk_x l/2} - jk_x sin(kl/2) - kcos(kl/2)}{k^2 - k_x^2} \quad (6)$$

$$A_y = I_0 \frac{\mu e^{-jkr}}{4\pi r} \frac{ke^{-jk_y l/2} + jk_y sin(kl/2) - kcos(kl/2)}{k^2 - k_y^2}. \quad (7)$$

In order to evaluate the far-field, first the magnetic potential $\mathbf{A}$ is transformed from Cartesian system to spherical coordinates as

$$A_\theta = A_x cos(\theta)cos(\phi) + A_y cos(\theta)sin(\phi) \quad (8)$$

$$A_\phi = -A_x sin(\phi) + A_y cos(\phi). \quad (9)$$

In turn the electric ($\mathbf{E}$) and magnetic field ($\mathbf{H}$) intensities read

$$\vec{\mathbf{E}} = -j\omega(\hat{\theta}A_\theta + \hat{\phi}A_\phi) \quad (10)$$

$$\vec{\mathbf{H}} = \eta\hat{r} \times \vec{\mathbf{E}} \quad (11)$$

where $\eta = 120\pi$ Ω is the intrinsic-wave impedance of free space.

The far-field generated by the other Γ–dipoles (#2, #3, and #4) can be derived through coordinate transformation, but the appropriate current direction must be carefully considered as in Fig. 1 (red arrows). For completeness and better understanding the sinusoidal distributions similar to (2) for all four dipoles are depicted in Table II. The corner dipoles have different bounds in integrals of the (4) and (5). A general solution of the integral of (3) for every dipole can be derived using two sign parameters, namely, as $S_1 = \pm 1$ and $S_2 = \pm 1$ while assuming unitary amplitude for the excitation current

$$\mathbf{A}_x^i = S_1 \frac{\mu e^{-jkr}}{4\pi r} \frac{ke^{jS_1 k_x l/2} - jS_1 k_x sin(kl/2) - kcos(kl/2)}{k^2 - k_x^2} \quad (12)$$

$$\mathbf{A}_y^i = S_2 \frac{\mu e^{-jkr}}{4\pi r} \frac{ke^{-jS_2 k_y l/2} + jS_2 k_y sin(kl/2) - kcos(kl/2)}{k^2 - k_y^2} \quad (13)$$

where the parameters take the values $(S_1, S_2) = (+, +)$, $(-, +)$, $(-, -)$, and $(+, -)$, respectively, for the Γ–dipoles #1, #2, #3, and #4 setting as reference the dipole #1. The rotation and mirroring of the coordinate system of Γ–dipole #1 is another way to derive (12) and (13).
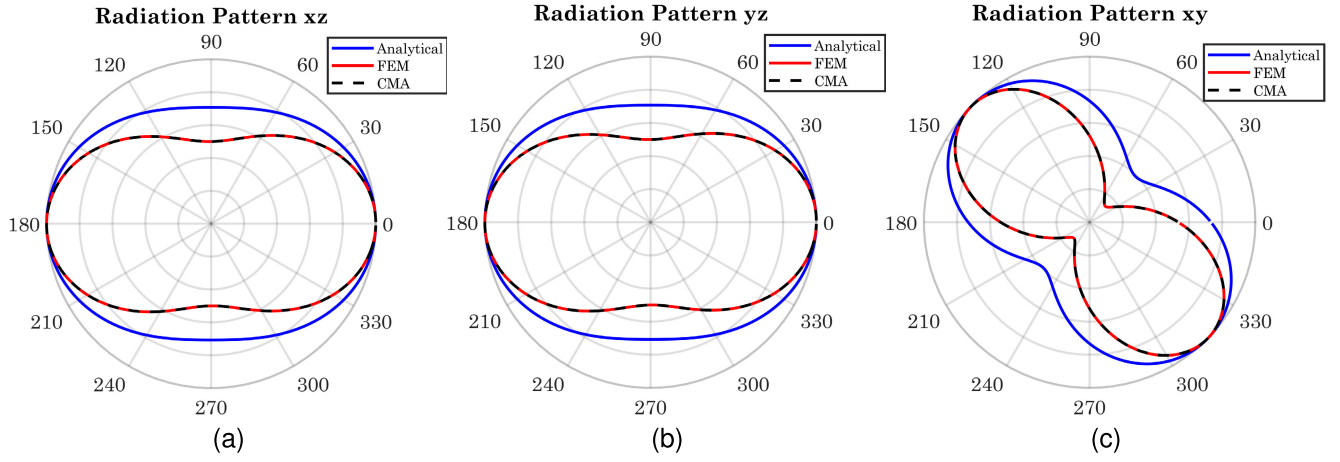
Fig. 4. Comparison of analytical and numerical (CMA and FEM) normalized radiation patterns (linear scale) of the Γ–dipole #1 in (a) xz, (b) yz, and (c) xy planes.

TABLE II
THEORETICAL CURRENT DISTRIBUTION OF THE FOUR CORNER DIPOLES
(POSITIVE $\hat{x}'$ POINTS TO THE RIGHT AND POSITIVE $\hat{y}'$ UPWARD)

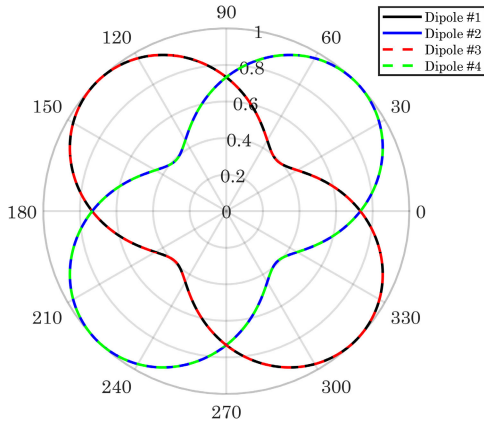| Dipole	$\hat{x}$ branch	$\hat{y}$ branch	Filamentary Current I_e
#1	(a)	(d)	$\hat{x}I_0 sin[k(\frac{l}{2} - x')], \quad 0 \le x' \le l/2 \ (a)$
#2	(b)	(d)	$\hat{x}I_0 sin[k(\frac{l}{2} + x')], \quad 0 \le x' \le l/2 \ (b)$
#3	(a)	(c)	$\hat{y}I_0 sin[k(\frac{l}{2} - y')], \quad 0 \le x' \le l/2 \ (c)$
#4	(b)	(c)	$\hat{y}I_0 sin[k(\frac{l}{2} + y')], \quad 0 \le x' \le l/2 \ (d)$

Fig. 5. Normalized radiation pattern (linear scale) of every dipole in xy plane derived from the analytical expression.

2) Γ–Dipole Far-Field Study: Let us now study the characteristics of the produced field of the Γ–dipole. The radiation pattern of dipole #1 is extracted numerically (CMA and FEM with source) and analytically and compared in Fig. 4. The dominant mode's radiation eigen-pattern presented in Fig. 4 is almost identical to the corresponding pattern when a voltage source is sought in the FEM. The numerical and analytical results are in relatively good agreement confirming that the approximation of the current distribution as sinusoidal is correct.

The radiation patterns of all four dipoles are shown in Fig. 5 where it is observed that they result from the appropriate rotation of that of #1 dipole. The rotation is performed in the xy plane, azimuthal angle (ϕ), as $\phi \to \phi - n\pi/2$ for $n = 2, 3, 4$. Namely, dipole #2 is a 90°-rotated, dipole #3 180°-rotated, and dipole #4 270°-rotated (right-handed) with

respect to dipole #1. So the radiation patterns of the dipoles in xy plane are rotated by the corresponding angle as seen in Fig. 5 where due to symmetry the dipoles have similar radiation patterns in pairs. The radiation patterns in xz and yz remain the same because the transformation applies only to the xy plane.

C. Γ–Dipole Array Far-Field

Let us now proceed in the study of the far-field of Γ–dipole array depicted in Fig. 2(b).

1) Closed Form Solution of the Γ–Dipole Array: Having the radiation pattern of each dipole, the next step is to compute the array's radiation pattern. The magnetic potential **A** for a general array (arbitrarily located or oriented elements) of N elements is given according to [29] in the following:

$$\vec{A} = \frac{\mu e^{-jkr}}{4\pi r} \sum_{i=1}^{N} \left\{ \bar{I}_i(\vec{r}_i) e^{j\vec{k}\cdot\vec{r}_i} \iiint_{V_i'} \vec{J}_{i,norm}(\vec{r}'') \right.$$
$$\left. \cdot e^{j\vec{k}\cdot\vec{r}''}(d\vec{r}'')^3 \right\} \quad (14)$$

where $\bar{I}_i(\vec{r}_i) = |I_i|e^{ja_i}$ is the complex excitation current, $\vec{r}_i$ the position vector of the ith element in the subvolume V_i', $\vec{J}_{i,norm}$ the normalized current of each element as given in Table II.

The magnetic potential **A** can be further simplified using (12) and (13) to replace the integrals of (14). Considering a common phase center $(0, 0)$ for the four element array as in Fig. 2(b), their position vector can be written as

$$\vec{r}_i = x_i\hat{x} + y_i\hat{y} \quad (15)$$
$$x_i = S_1^i G \quad \text{and} \quad y_i = S_2^i G \quad (16)$$
$$\vec{k}\cdot\vec{r}_i = kx_i sin\theta cos\phi + ky_i sin\theta sin\phi = k_x x_i + k_y y_i. \quad (17)$$

The magnetic vector potential for the array reads

$$A_x = \sum_{i=1}^{N} \left\{ |I_i|e^{ja_i} e^{j\vec{k}\cdot\vec{r}_i} A_x^i \right\} \quad (18)$$

$$A_y = \sum_{i=1}^{N} \left\{ |I_i|e^{ja_i} e^{j\vec{k}\cdot\vec{r}_i} A_y^i \right\} \quad (19)$$
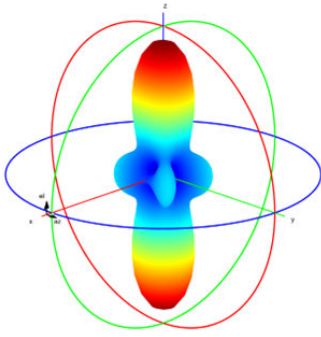
Fig. 6.   Linear power pattern for the $(1, -1, -1, 1)$ excitation quartet.

where $G = L_p + g/2$ as defined in Fig. 1 and $(S_1^i, S_2^i) = (-, +), (++), (+, -)$, and $(-, -)$ for $i = 1 - 4$ dipoles. The far-field of the array can be obtained by substituting (18) and (19) into (8)–(10).

2) Γ–Dipole Array Far-Field Study: Note that, care is needed to assess the excitation necessary for proper array beamforming. This is due to the fact that the proposed antenna is not a conventional array of one type of radiator. For example, for broadside radiation, one should enforce the following $(+1, -1, -1, +1)$, [and, of-course due to, the Γ–dipole array's, $90°$ rotational symmetry, also $(+1, +1, -1, -1)$, $(-1, +1, +1, -1)$, and $(-1, -1, +1, +1)$], quartet excitation rather than the uniform $(+1, +1, +1, +1)$ one. The respective results are presented in Fig. 6.

For the uniform array with four elements, excitation amplitudes $|I_i| = I_0 = 1$ and phases $a_1 = 180°$, $a_2 = 180°$, and $a_3 = 0°$, $a_4 = 0°$ the analytical expression is utilized, while the array is simulated in CST studio [28]. A good agreement between the analytical and numerical normalized radiation patterns is depicted in Fig. 7. The parameters used for the simulation and analytical solution are presented in Table III.

IV. ANTENNA FABRICATION AND CHARACTERIZATION

In this section, we provide details about the array fabrication and characterization.

A. Technical Specifications

The technical specifications of the designed antenna array are the compact size (fitting in most IoT devices), the operation in the ISM band (2.4–2.489 GHz), the capability of detecting every kind of polarization (linear, circular, and elliptical), as well as performing DoA and beamforming. To fulfill the above we propose the Γ–dipole array antenna. The fabrication details are given next.

B. Prototype

Two fabrication options are investigated for the Γ–dipole array: the dipoles can be either cylindrical metallic conductors just like conventional dipoles or printed on the flexible dielectric. In Fig. 8(a), the cylindrical metallic wire conductors array is presented. The dipoles are placed or printed above a thin (1 mm) flexible dielectric plate such as PVC ($\epsilon_r = 4$) enabling the application in any IoT device independent of size and geometry. Each branch of the four Γ–dipoles has a length

TABLE III
DIMENSIONS OF PROPOSED ANTENNA (TWO OR FOUR ELEMENTS) WITH
EITHER WIRE OR PRINTED CONDUCTORS AS SEEN IN FIG. 1

(2/4 elements)	Printed	Wire
Parameter	Dimensions (mm)	
W	25/75	30/80
T	75/75	80/80
W_p	1.93/1.93	1/1
L_p	23.4/23.4	23/23
L_g	2/2	2/2
h	1/1	1/1
g	2/20.1	5/25

approximately of $\lambda_0/4 = 30$ mm at the central frequency (2.48 GHz). In the wire dipole antenna choice, the copper conductors are chosen with a diameter of $\sim$1 mm to match the central conductor of the SMA coaxial probe feed.

A microstrip-printed antenna configuration was prepared and tested [Fig. 8(b)]. An ordinary commercial available FR-4 substrate with relative permittivity $\epsilon_r = 4.1$ and $tan\delta = 0.025$ was utilized. Each printed branch length is $\lambda_g/4 \approx 23.4$ mm so as to resonate at 2.48 GHz. Notably, the effective dielectric constant for dipoles printed on a dielectric substrate (without ground plane) can be approximated by $\epsilon_{reff} = (\epsilon_r + 1)/2$. Thus, the guided wavelength is estimated as $\lambda_g = \lambda_0/\sqrt{\epsilon_{reff}}$. The final dimensions of the fabricated antennas, obtained after a parametric study, are given in Table III.

C. S-Parameters Characterization

The measurements of the S-parameters were carried out using a vector network analyzer HP 8510C. The symmetry of the four-element antenna array permits to calculate/measure only three of the total 16 S-parameters. Namely, for each dipole, say the #1 (Fig. 1), apart from the input reflection coefficients ($S_{ii} = \Gamma$) and the coupling term ($S_{31} = T_2$) to the antidiametrical element, the coupling terms to the neighboring elements (S_{41} and S_{21}) will be the same ($=T_1$). The resulting S-parameters matrix reads

$$\mathbf{S} = \begin{bmatrix} \Gamma & T_1 & T_2 & T_1 \\ T_1 & \Gamma & T_1 & T_2 \\ T_2 & T_1 & \Gamma & T_1 \\ T_1 & T_2 & T_1 & \Gamma \end{bmatrix}. \tag{20}$$

Scattering parameter data from simulation utilizing the commercial electromagnetic software CST studio [28] and measurements are depicted in Fig. 9 for both antennas. The two antenna's configurations are operating at a central frequency 2.48 GHz with a bandwidth of 350 MHz or fractional bandwidth 14%. The coupling terms T_1 and T_2 within this range are below -10 dB.

In both cases, the measured S-parameters are in acceptable agreement with the simulated ones, especially within the operational frequency band with a maximum deviation 20% for the wire and 23% for the printed dipoles. The cut-of-band deviation is higher reaching 50%, especially for the reflection coefficients and this can be attributed to higher losses. However, this does not affect the antenna operation. In addition, the deviation between simulation and measurements is lower for the printed antenna as compared to the wire antenna due to the poor alignment of wire
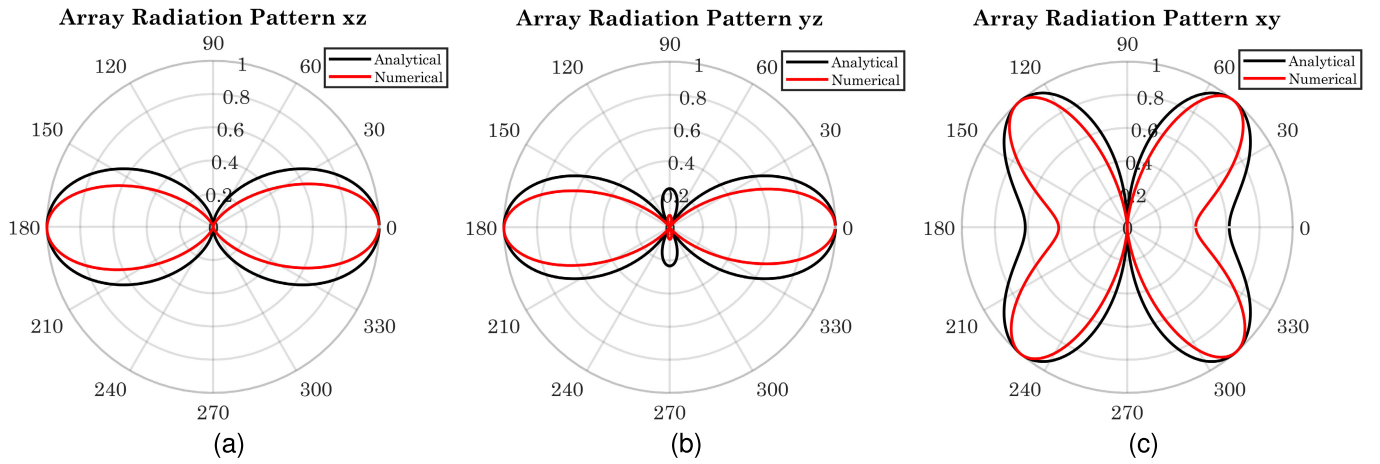
Fig. 7. Comparison of analytical and numerical normalized radiation patterns of the array in uniform excitation $|I_i| = 1$ and $a_1 = a_2 = 180°$ and $a_3 = a_4 = 0°$. (a) xz, (b) yz, and (c) xy planes.
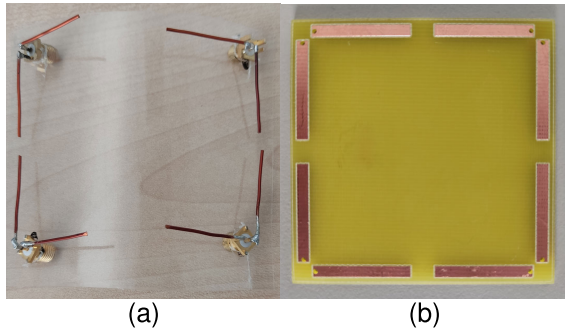

Fig. 8. Top view of the fabricated antenna in (a) dipole and (b) printed configuration.

Fig. 9. Antenna's measured and simulated S-parameter values (Γ, T_1, T_2) (a) wire and (b) printed Γ–dipole array.

dipoles. Even, though the wire dipoles antenna is operating satisfactorily and this is an indication of its robustness against any fabrication imperfections including its curvature.

D. Far-Field Characterization

In order to characterize the produced far-field, measurements were conducted in the Microwave Lab's anechoic chamber using a vector network analyzer. Due to symmetry and space reasons, one subset of those is discussed here which is relative to one Γ–dipole far-field. There are three planes of interest, that can characterize the whole far-field. With reference to dipole #1 of Fig. 2(a), the far-field radiation on $\phi = -45°$, $\phi = +45°$, and the $\theta = 90°$ planes, where the ϕ-vector field is relevant, was investigated.

For the $\phi = -45°$ plane normal (case 1), the far-field is proved to be practically omnidirectional, as it was expected. Also, for the $\phi = +45°$ plane (case 2), the far-field is proved to be practically insignificant. Last, case 3 results, apart from some minor discrepancies due to anticipated measurement inaccuracies, verify the field presented in Fig. 5. Note that, having verified those then due to [30] the multibeam capability of the array is secured.

V. ANTENNA VERIFICATION

Various aspects of the antenna's performance, like polarization, beamforming, DoA agility, and also deformation

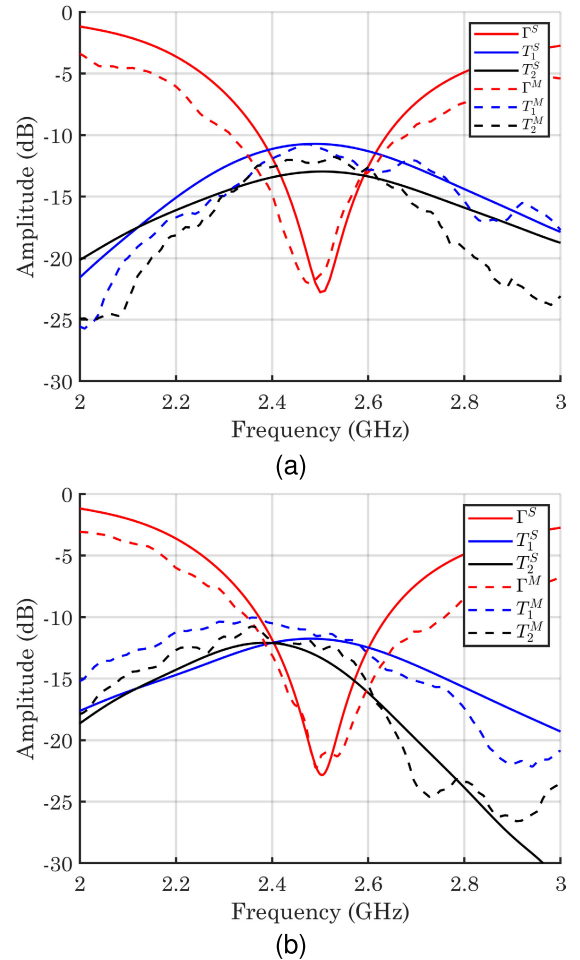resilience are presented herein in detail providing mathematical results, simulation, and measurement data.

A. All Polarization Property

In this section, the all-polarization property is demonstrated both in receiving (Rx) and transmitting (Tx) functions.

TABLE IV
SIMULATED AND MEASURED INDUCED VOLTAGE OF DIPOLES #1 AND #2 FOR FIVE DIFFERENT POLARIZATIONS OF A z-AXIS
PROPAGATING PLANE WAVE OF WIRE DIPOLE ANTENNA

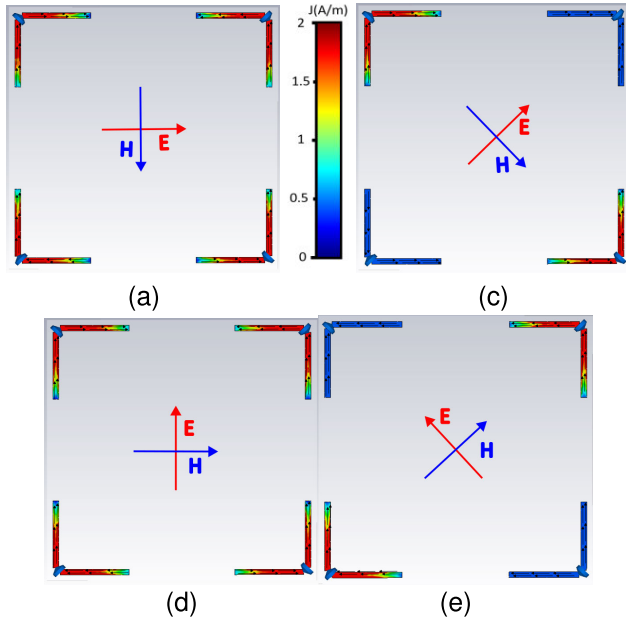| Polarization	Sim. Dipole #1/#3 (V)	Sim. Dipole #2/#4 (V)	Meas. Dipole #1/#3 (V)	Meas. Dipole #2/#4 (V)
Horizontal	1.08	1.08	0.92	0.85
Linear $\pi/4$	0.05	1.06	0.1	0.87
Vertical	1.08	1.08	0.90	0.91
Right Hand Circular	1.37	1.37	1.21	1.32
Left Hand Circular	1.37	1.37	1.17	1.33

Fig. 10. Excited surface currents of the antenna (Fig. 1) from a normally incident $\hat{z}$-propagating linearly polarized wave with different polarization angles (a) horizontal or at 0°, (b) obliquely at 45°, (c) vertically or at 90°, and (d) obliquely at 135°.

Since the antenna is reciprocal only the receive function will be analyzed explicitly.

1) Rx-Function: For the receiving case, the all-polarization property is best demonstrated following the voltage open circuit formula, (1). Since, as is verified in Table I, the antenna vector length $\vec{h}$ is written as a linear combination of two independent vectors ($\hat{\theta}$ and $\hat{\phi}$) indeed the antenna adequately receives/detects all-polarization signals. This statement holds for both the four-element but also for any two, successive-element subarray. For example, the receiving function of the #1, #2 subarray was tested through simulations and found capable of detecting any type of CP, without any degradation in its response as presented in Table IV.

To elaborate further, the resulting surface currents, upon a general incident field, are depicted in Fig. 10, where one may observe that the flowing current is stronger along the branches parallel to the electric field, as expected. However, whenever a current is induced in one branch this builds a voltage at the feeding gap, which will cause the current to continue flowing on the other branch even thought that is perpendicular to the electric field [Fig. 10(a)–(d)]. What is again interesting to observe in Fig. 10(c) and (e) is that the oblique electric field direction generates pointing toward the feeding gap of dipoles (#1, #3) and (#2, #4), respectively. The components

induce equal surface currents flowing toward the feeding gap, which in turn results to null voltage and minimum total current. Explicitly, when only dipole #1 (Fig. 1) is considered and for LP, nulls of radiation pattern occur when the electric field is oriented toward direction $\theta = 3\pi/4, 7\pi/4$ (Figs. 5 and 11).

The solution to this problem is to include a second Γ–dipole, e.g., #2 rotated by 90°, with respect to the #1. This one displays minimum induced voltage when the incoming wave incidents at angles $\pi/4$ and $5\pi/4$, as depicted in Figs. 5 and 11(a). Thus, when dipoles #1 and #2 are combined the radiation pattern becomes nearly isotropic, enabling the transmitting/receiving signal in every azimuth and elevation angle as seen in Figs. 5 and 11(b). Namely, by combining the voltages of the dipoles #1 and #2, all polarization detection will be achieved using only two elements. The same properties are observed when the two lower dipoles, #3 and #4 are combined due to symmetry along the x-axis. In addition, this property is exhibited by the two vertical pairs (#1, #3) or (#2, #4) as well.

Overall, the total induced voltage at each one of Γ–dipoles #1, #2 and their total sum versus the polarization's direction (electric field orientation) is illustrated in Fig. 11(a). Γ–dipole #1 presents a null toward $\phi = 3\pi/2$, while dipole #2 a null at $\phi = \pi/2$. Thus their total sum is always nonzero providing signal detection for any case. From the same point of view, circularly or elliptically polarized waves are more favorable or always detected since their electric field angle rotates in time as $\phi = \omega t$ and this also is validated in Fig. 11(b).

2) Tx-Function: Analogously, the transmitting antenna can support both CP and LP when fed with appropriate phase difference in each port. A case of vertical LP is achieved when the dipoles #1 and #4 excited with 180° phase difference compared to the other two dipoles (#2 and #3). On the other hand, a circularly polarized wave can be radiated if the phase difference of the opposite corner dipoles (e.g., #1 and #3) is 180° and the phase difference of the neighboring dipoles (e.g., #1 and #2) is 90°. As expected from the conventional cross dipole the circular wave is right-hand CP (RHCP) polarized in one direction and left-hand CP (LHCP) in the other based on the sign of phase difference. Exciting the dipoles with the following phase $\phi = 0°$, $\phi = -90°$, $\phi = 180°$, and $\phi = 90°$ the forward is RHCP while the backward wave is LHCP.

B. Beamforming

The conventional theory of rectangular arrays (that builds beam-steering on pattern multiplication) is not applicable for beamforming on the proposed array. This is due to the fact that the elements are of the same type but for the array, rotated
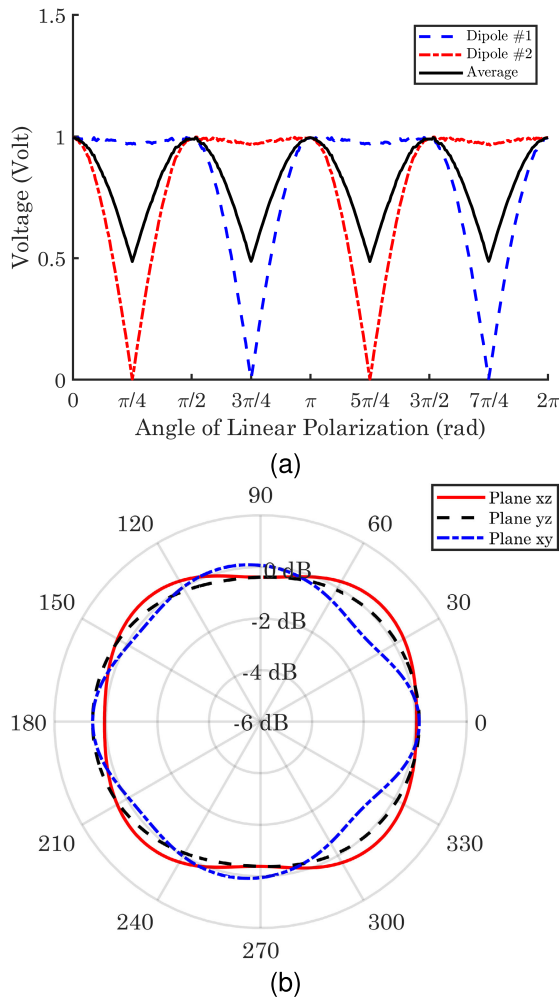
(a)

(b)

Fig. 11. (a) Excited voltages in every dipole and the total added voltage of dipoles #1 and #2 in comparison with the angle of the linear polarized electromagnetic wave. (b) Two-dipole array's radiation pattern when the dipoles are fed with excited currents with a phase difference of 180° of xz, yz, and xy plane. The amplitude variation in 3-D space is lower than 1 dB.

clones of them are used. This, although complicates analysis, equips the Γ–dipole array with unique capabilities. For near broadside radiation, one can employ excitation quartets that transform the array into a uniform planar one. For the near endfire case of radiation, relative excitations, transform the Γ–dipole array to an UCA. After this distinction is made, one can employ UPA beamforming techniques for near-broadside radiation and UCA beamforming techniques for near-endfire radiation scenarios. The following analysis will further elaborate on those facts.

1) Omnidirectional Pattern: Interestingly, the appropriate excitation of either a pair or all four dipoles of Fig. 1 may offer an omnidirectional or a controllable directional radiation pattern. It is useful first to recall that a single crossed dipole presents an omnidirectional pattern but only in the xz plane [31]. The direction of currents along the four Γ–dipoles' branches is depicted in Table V. One may intuitively observe that for the excitation $[I_i] = (1, -1, 1, -1)$ the combination of the dipoles may virtually synthesize a rectangular loop antenna, which offers a quasi-omnidirectional pattern along xy plane [Fig. 11(b)].
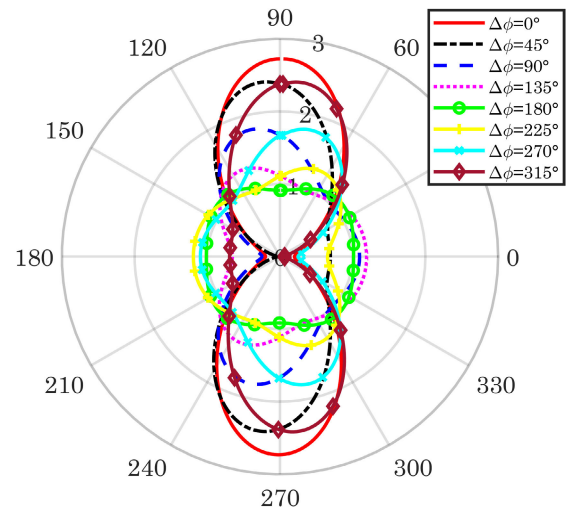

Fig. 12. Radiation pattern of two-dipole array in plane xz for different phase differences between the dipoles #1 and #2.

The individual Γ–dipoles' branches, (depicted in 5), when excited with the same current ($I_i = +1$) may intuitively conclude that any pair of consecutive dipoles (i, $i + 1$) yields to a quasi-isotropic pattern. However, the electric fields generated by a pair of consecutive dipoles are anti-parallel (a fact not illustrated in the patterns of Fig. 5) due to the opposite direction of the inline currents. Hence, an omnidirectional pattern is expected when the consecutive (i, $i + 1$) Γ–dipoles are fed with $\Delta\phi = 180°$ phase difference as $(I_i, I_{i+1}) = (+1, -1)$. Overall, consecutive Γ–dipoles fed with $\Delta\phi = 180°$ present unidirectional in-line currents and anti-parallel perpendicular currents to yield a 3-D isotropic radiation pattern. On the contrary, the in-phase $\Delta\phi = 0°$ excitation presents anti-parallel in line currents and parallel perpendicular currents (monopoles array at $\lambda_0/2$ distance) to yield a broadside directional pattern (Fig. 12). What was unexpected and impressive is the 3-D almost perfect isotropic radiation pattern observed for $\Delta\phi = 180°$ shown in Fig. 11(b) with only a 0.8 dB fluctuations.

2) 2-D Beamforming With a Pair of Γ–Dipoles: The next task is to test through simulations the beamforming characteristic of the two-dipole array. For this purpose, the pair of Γ–dipoles #1, #2 are excited with the same amplitude but a phase difference varying from 0° to 315°. The resulting patterns are indicated in Fig. 12, it starts from the broadside at $\Delta\phi = 0°$, while at $\Delta\phi = 180°$ the radiation pattern became omnidirectional (isotropic in 3-D). The directivity varies from 0.541 to 4.36 dBi as seen in Figs. 11(b) and 12. For $\Delta\phi = +90°$, the beam is tilted slightly to 13° while the high axial ratio of 0.5 dB in 0° indicates that the polarization can be approximated as CP.

3) Circular Polarization: For the above $\Delta\phi = +90°$, we may prove the type of CP. Let the currents exciting Γ–dipoles #1 and #2 as $I_1 = I_0(\hat{x} + \hat{y})$ and $I_2 = I_0(-\hat{x} + \hat{y})e^{j90}$, by combining the vertical branches of the two dipoles as $I_{1x} + I_{2y} = I_0(\hat{x} + j\hat{y})$ and $I_{2x} + I_{1y} = I_0(-j\hat{x} + \hat{y}) = -jI_0(\hat{x} + j\hat{y})$ is observed that both yield a LHCP. This can be generalized for any pair of consecutive Γ–dipoles

TABLE V
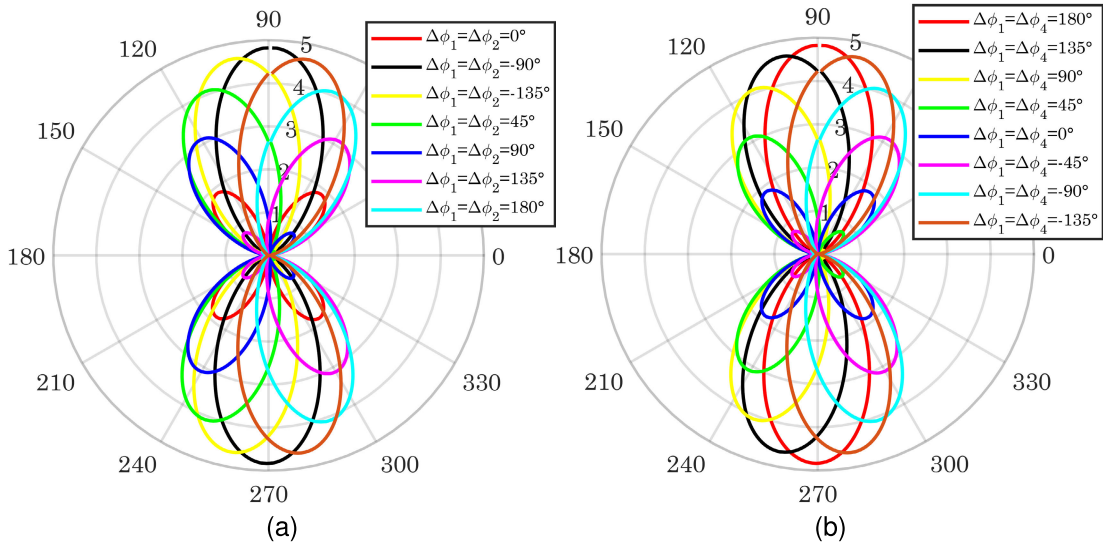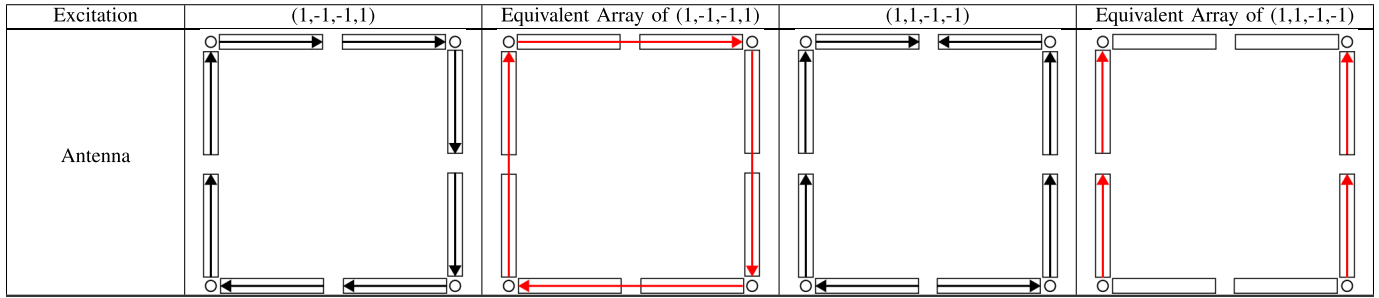EXCITATION CURRENTS RESULTED Γ−DIPOLE ARRAY EQUIVALENCE

Excitation	(1,-1,-1,1)	Equivalent Array of (1,-1,-1,1)	(1,1,-1,-1)	Equivalent Array of (1,1,-1,-1)
Antenna				

Fig. 13. Radiation pattern (linear scale) of the antenna on (a) primary E-field cut (plane xz) and (b) H-field cut (plane yz) for different phase differences between the dipoles #1, #2, and #4.

which yield to LHCP for $\Delta\phi = +90°$, but the same is also expected when all four dipoles are fed. It can be easily proved that feeding with a $\Delta\phi = -90°$ between consecutive dipoles yields RHCP. It is important to note that the above claims hold for the positive $\hat{z}$-axis or the front beam. On the contrary, looking toward the negative $-\hat{z}$-axis or toward the back lobe the polarization is reversed. This observation is in accordance with the behavior of crossed dipoles [31].

4) 3-D Beamforming With Four-Element Array: Overall, all four Γ−dipoles can be excited simultaneously to yield a directional beam steering in both azimuth and elevation. For example, to take an approximately frontal radiation pattern one needs to feed two diagonally placed Γ−dipoles with phase difference 180°. This can be explained with the equivalent currents presented in Table V where an equivalent two-dipole array is displayed.

It is chosen to feed the dipoles only with discrete phase values (45°, 90°, 135°, and 180°) to observe the bend of the main radiation lobe. It is determined that feeding with phase difference between two dipoles the beam can turn based on the pair of chosen dipoles. If we choose the dipoles (#1 and #4) or (#2 and #3) the beam can turn in elevation angle just like in Fig. 13(a). Respectively, feeding the dipoles (#1 and #2) or (#3 and #4) the main lobe will turn in azimuth angle just

like Fig. 13(b). The radiation patterns are depicted using linear scaling for visualization purposes in order for the beams to be distinguishable.

From the Radiation Patterns in the linear scale of Fig. 13 someone can observe that the total scanning range is approximately (−30°:+30°) both in azimuth and elevation angles. Although, increasing the angle of the main beam (either in azimuth or elevation angles) the amplitude of the main lobe is decreasing. The main reason behind this phenomenon is the different structures between the elements of the array that generates parasitic lobes in other directions. However, the main lobes in different angles have higher amplitude than that of the frontal lobe, making the beam forming efficient. This is where the Γ−dipole array to UPA approximate equivalence breaks down. The various excitations of the four-element array are summarized in Table VI, where the beam maximum orientation (ϕ_0, θ_0) as well as their beamwidth, sidelobe level (SLL) and gain are depicted.

C. Direction of Arrival

It is common sense that to perform a DoA function two overlapping radiated beams with offset maxima are needed. In Section V-B and particularly Section V-B4 proved the

TABLE VI
PHASE OF EXCITATION CURRENTS OF EVERY DIPOLE AND THEIR SIMULATED MAIN LOBE AMPLITUDES, GAIN,
BEAMWIDTH, SLL, AND ANGLES (AZIMUTH AND ELEVATION), RESPECTIVELY

Direction	$\Delta\phi_1$	$\Delta\phi_2$	$\Delta\phi_3$	$\Delta\phi_4$	Azimuth Angle	Elevation Angle	Max Amplitude	Gain	Beamwidth	SLL
1R	$-135°$	$0°$	$0°$	$-135°$	$101°$	$90°$	4.65	6.67 dB	57.4°	–
2R	$-90°$	$0°$	$0°$	$-90°$	$111°$	$90°$	4.09	6.12 dB	54.9°	$-14\ dB$
3R	$-45°$	$0°$	$0°$	$-45°$	$121°$	$90°$	3.12	4.93 dB	50.1°	$-6.1\ dB$
1L	$135°$	$0°$	$0°$	$135°$	$79°$	$90°$	4.65	6.67 dB	57.4°	–
2L	$90°$	$0°$	$0°$	$90°$	$69°$	$90°$	4.09	6.12 dB	54.9°	$-14\ dB$
3L	$45°$	$0°$	$0°$	$45°$	$59°$	$90°$	3.12	4.93 dB	50.1°	$-6.1\ dB$
1U	$135°$	$135°$	$0°$	$0°$	$90°$	$101°$	4.65	6.67 dB	57.4°	–
2U	$90°$	$90°$	$0°$	$0°$	$90°$	$111°$	4.09	6.12 dB	54.9°	$-14\ dB$
3U	$45°$	$45°$	$0°$	$0°$	$90°$	$121°$	3.12	4.93 dB	50.1°	$-6.1\ dB$
1D	$135°$	$-135°$	$0°$	$0°$	$90°$	$79°$	4.65	6.67 dB	57.4°	–
2D	$-90°$	$-90°$	$0°$	$0°$	$90°$	$69°$	4.09	6.12 dB	54.9°	$-14\ dB$
3D	$-45°$	$-45°$	$0°$	$0°$	$90°$	$59°$	3.12	4.93 dB	50.1°	$-6.1\ dB$
LHCP-RHCP	$0°$	$-90°$	$180°$	$-90°$	$90°$	$90°$	4.83	6.84 dB	57.9°	–
RHCP-LHCP	$0°$	$-90°$	$180°$	$90°$	$90°$	$90°$	4.83	6.84 dB	57.9°	–
Broadside	$0°$	$0°$	$180°$	$180°$	$90°$	$90°$	4.83	6.84 dB	57.9°	–
Omnidirectional	$180°$	$0°$	$180°$	$0°$	–	$0°$	1.25	0.95 dB	–	–

beamforming (steered) beams in both azimuth and elevation, thus DoA in 3-D can be supported.

As usual, DoA is performed by exploiting the beamforming capability. In Section V-B, the beamforming capability is proved for the transmission function by simultaneously activating either two (2-D) or four Γ–dipoles (3-D). For the DoA function, the directional beams must be virtually synthesized during the receive function and they must be identical to their transmit counterparts due to the reciprocity principle. For this purpose, the above experiment is carried out and the temporal signals received at the terminals of each Γ–dipole are subjected to the appropriate phase lag in order to synthesize the response of successive beams. In turn, the resulting signals for successive beams are compared in terms of amplitude and/or phase in order to estimate the angle (direction) of arrival-incidence of the incoming wave generated by the source to be localized. Recall that for amplitude comparison the reference direction (zero angle) is along the intersection of the two successive beams where their gain is equalized. On the contrary, for phase comparison, the reference is along the direction perpendicular to the axis passing through the phase center (gap) of the two Γ–dipoles.

A simulation verifying this capability of the antenna is conducted. Assuming a linear polarized ($\hat{y}$) plane wave propagating in different azimuth angles (scan from $-30°$ to $30°$ when 0 is the $\hat{z}$ propagating wave), a diagram of the excited voltage's amplitude of the beams versus the direction angle was derived and presented in Fig. 14 for two beams #1 and #2 of the array and their ratio. The selected beams are the 2R and 2L based on Table VI which display their maxima in $111°$ and $69°$, respectively. We decided to choose these beams and not the 3L and 3R because the latter presented poor SLL and gain, degrading the accuracy of the DoA. To test the DoA capability, it was assumed that the incoming electromagnetic plane wave has $0°$ in elevation angle. Carefully observing the ratio between the two beams (ratio curve) in Fig. 14, a monotonous but not linear behavior is noticed. This means that it is plausible to utilize a lookup table to correlate the propagating wave's angle of incidence with the ratio of beams' amplitude (Fig. 14). Another possibility
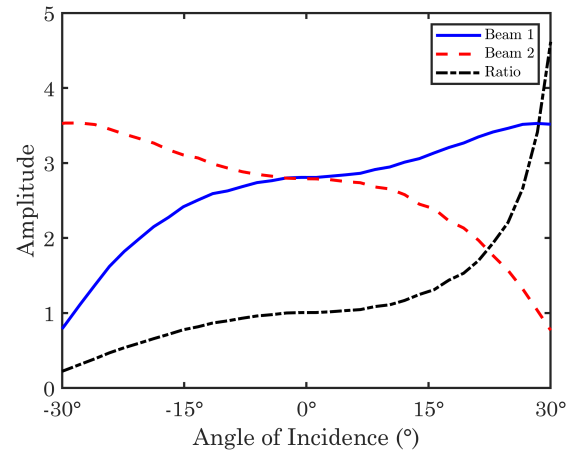

Fig. 14. Simulated results of the amplitude of the beams #1 and #2 when linearly polarized ($\hat{y}$) plane electromagnetic wave is propagating at obligue azimuth angle.

is to apply a curve-fitting technique targeting an error of $1°$.

Finally, measurements were performed testing the antenna's ability to detect the DoA of an incoming plane wave using the amplitude scheme. The DoA functionality would permit the IoT devices to detect nearby devices. Note that the antenna presents a large half-power beamwidth angle, so the DoA will have better accuracy at close distances up to 40 m. This is not necessarily a bad approximation as most IoT devices will be placed in close proximity (e.g., sensors in a smart house). In this particular experiment, a close distance (5 m) was tested utilizing two software-defined radios (SDRs), a Hack RF One [32] and an Ettus Research USRP N210 [33]. The former is used as a receiver and the latter as a source of the plane wave produced by a directional horn antenna. Five cases were performed for the azimuth angle estimation, frontal radiation on the antenna ($0°$), radiation at an angle of $15°$ and $30°$ (right rotation), and radiation at an angle of $-15°$ and $-30°$ (left rotation) with respect to the frontal case. The experiment took place in a room with different furniture and electronic devices taking into account the different reflections that may happen in real IoT applications.

TABLE VII

MEASURED EXCITED VOLTAGE OF THE BEAMS #1 AND #2 OF WIRE DIPOLE ANTENNA FOR DIFFERENT ANGLE OF ARRIVAL OF A PLANE WAVE

Angle	Amp. Beam #1	Amp. Beam #2	Ratio V_1/V_2	Estimate Angle	Relative Error
$-30°$	3.36	1.12	3	$27.4°$	8.66 %
$-15°$	3.34	2.4	1.3917	$16.81°$	6 %
$0°$	2	2	1	$0°$	0 %
$+15°$	1.94	2.84	0.69	$-18°$	10 %
$+30°$	1.12	2.96	0.37	$-26.3°$	12.3 %

TABLE VIII

SIMULATED AND MEASURED EXCITED VOLTAGE OF ALL THE DIPOLES FOR FIVE DIFFERENT POLARIZATION OF A z-AXIS PROPAGATING PLANE WAVE FOR CURVED STRUCTURE OF FIG. 8(a)

Polarization	Sim. Dipole #1/#3 (V)	Sim. Dipole #2/#4 (V)	Meas. Dipole #1/#3 (V)	Meas. Dipole #2/#4 (V)
Horizontal	0.49	0.49	0.62	0.57
Linear $\pi/4$	0.92	0.9	0.8	0.69
Vertical	0.62	0.4	0.52	0.41
Right Hand Circular	0.55	1.35	0.62	1.2
Left Hand Circular	0.58	1.36	0.63	1.15

The amplitudes at the two beams, their ratio and the estimated angle of arrival based on the lookup table defined by the results of Fig. 14 are given in Table VII, respectively. The results show good accuracy with respect to the angle of incidence of the incoming wave. The amplitudes of the beams are normalized with respect to the broadside plane wave (0°) where a calibration procedure is conducted to minimize the difference in the response of the two SDRs. As expected from the results, the ratio between the beams' voltage gives relatively good results for these specific cases with small and tolerable errors 10%. However, the amplitude DoA is not as accurate as calculating the AoA but is a more convenient method to implement than the phase scheme. Furthermore, there are some inconsistencies between the right and left angles that may be caused by the different reflections and the antenna asymmetries caused by the fabrication errors. The corresponding results can be expected for the case of utilizing the beams U2 and D2 to estimate the elevation angle due to the symmetrical property along x and y-axes of the antenna.

D. Curved Geometry

The next question raised was whether this antenna will be capable of detecting any type of polarization when wrapped over a curved object-thing or when the object surface hosting the antenna could be distorted-bend. For this purpose, different bend antennas were tested through simulations.

For the convenience of simulations, it was assumed that the IoT device has a cylindrical shape with different radii where the antenna was placed using the flexible material as seen in Fig. 15. Four different test cases were simulated, specifically the antenna bend around a cylinder with a radius of 1.5, 3, 4.5, and 6 cm. The results are depicted in Fig. 15, where the all polarization capability of the antenna is clearly retained. The simulations assumed a $\hat{z}$ propagating plane wave with a magnitude of 100 V/m. The circular polarized electromagnetic wave was also tested that still can be detected without a sign of degradation. In order to validate this feature, an experiment was conducted where the antenna was wrapped around a cylindrical object. A SDR was utilized as a source and two SDRs as receivers. The excited voltages versus the LP angle
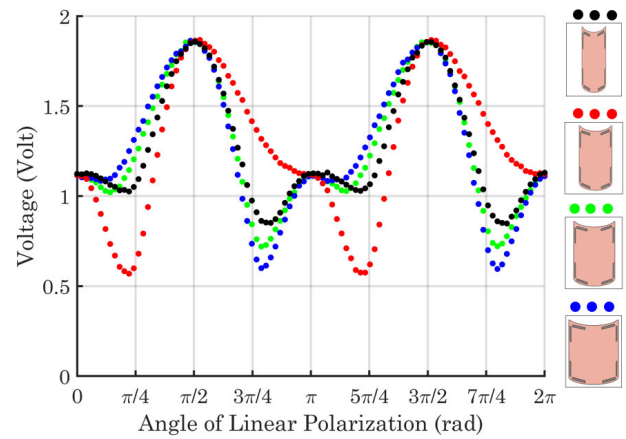

Fig. 15. Excited voltages in every dipole and the total added voltage of dipoles in comparison with the angle of the linear polarized electromagnetic wave in four different bend cases (hosting cylinder radius 1.5, 3, 4.5, and 6 cm).

are presented for five characteristic angles in Table VIII and compared against simulated results. The measured results were normalized to match with the simulated ones. It is crucial to notify that the beamforming and phase DoA estimation was not possible in the bend structure.

VI. CONCLUSION

A novel corner or Γ–dipole is proposed herein. Closed-form expressions are provided for its far-field and its behavior is checked using CMA. This is further exploited in a two- or four-element array. Explicitly, an all-polarization miniaturized antenna for the IoT applications is designed and fabricated. The combination of four dipoles on the same surface enables the ability to perform DoA and beamforming. The orthogonal position of the branches of each dipole provides with a characteristic of all polarization receiving and compact size fitting in almost every commercial sensor and actuator that lies inside a smart house. In addition, the antenna can be used as an RF harvester because even when it is bent the all-polarization property is maintained.

In a future extension of this effort, (a ground plane (PEC reflector) may be placed on the back side of the "thing,"

optimally parallel to the four dipoles at a quarter-wave distance), the antenna can become unidirectional. Furthermore, a printed version of the current antenna is going to be designed in order to be able to integrated in the device.

REFERENCES

[1] H. Gu, L. Ge, and J. Zhang, "A dual-band dual-polarized omnidirectional antenna," *Frontiers Phys.*, vol. 8, p. 598, Dec. 2020.

[2] M. S. Sadiq, C. Ruan, H. Nawaz, S. Ullah, and W. He, "Horizontal polarized DC grounded omnidirectional antenna for UAV ground control station," *Sensors*, vol. 21, no. 8, p. 2763, Apr. 2021. [Online]. Available: https://www.mdpi.com/1424-8220/21/8/2763

[3] S. M. Radha, M.-S. Lee, and I.-J. Yoon, "A compact broadband quasi-isotropic antenna for wireless energy harvesting applications," in *Proc. Int. Symp. Antennas Propag. (ISAP)*, Oct. 2022, pp. 137–138.

[4] D. Tyagi, S. Kumar, and R. Kumar, "Multifunctional antenna design for Internet of Things applications," in *Proc. 7th Int. Conf. Adv. Comput. Commun. Syst. (ICACCS)*, vol. 1, Mar. 2021, pp. 557–560.

[5] N. L. Johannsen, N. Peitzmeier, P. A. Hoeher, and D. Manteuffel, "On the feasibility of multi-mode antennas in UWB and IoT applications below 10 GHz," *IEEE Commun. Mag.*, vol. 58, no. 3, pp. 69–75, Mar. 2020.

[6] N. Kishore and A. Senapati, "5G smart antenna for IoT application: A review," *Int. J. Commun. Syst.*, vol. 35, no. 13, Sep. 2022, Art. no. e5241, doi: 10.1002/dac.5241.

[7] T. K. L. Hui, R. S. Sherratt, and D. D. Sánchez, "Major requirements for building smart homes in smart cities based on Internet of Things technologies," *Future Gener. Comput. Syst.*, vol. 76, pp. 358–369, Nov. 2017. https://www.sciencedirect.com/science/article/pii/S0167739X16304721

[8] C. L. Athanasiadis et al., "A smart energy management system for elderly households," in *Proc. 57th Int. Universities Power Eng. Conf. (UPEC)*, Aug. 2022, pp. 1–6.

[9] Y.-F. Lin, S.-A. Yeh, H.-M. Chen, and S.-W. Chang, "Design of an omnidirectional polarized RFID tag antenna for safety glass applications," *IEEE Trans. Antennas Propag.*, vol. 60, no. 10, pp. 4530–4537, Oct. 2012.

[10] S. Wang and H.-Y. Chang, "A 3D rectenna with all-polarization and omnidirectional capacity for IoT applications," in *IEEE MTT-S Int. Microw. Symp. Dig.*, Aug. 2020, pp. 1188–1190.

[11] N. P. Lawrence, B. W.-H. Ng, H. J. Hansen, and D. Abbott, "Analysis of millimetre-wave polarization diverse multiple-input multiple-output capacity," *Roy. Soc. Open Sci.*, vol. 2, no. 12, Dec. 2015, Art. no. 150322, doi: 10.1098/rsos.150322.

[12] N. P. Lawrence, H. Hansen, and D. Abbott, "Tri-orthogonal polarization diversity for 5G networks," *Trans. Emerg. Telecommun. Technol.*, vol. 27, no. 7, pp. 992–999, Jul. 2016, doi: 10.1002/ett.3042.

[13] B. N. Getu and J. B. Andersen, "The MIMO cube—A compact MIMO antenna," *IEEE Trans. Wireless Commun.*, vol. 4, no. 3, pp. 1136–1141, May 2005.

[14] J. X. Yun and R. G. Vaughan, "Slot MIMO cube," in *Proc. IEEE Antennas Propag. Soc. Int. Symp.*, Jul. 2010, pp. 1–4.

[15] D. Piao and Y. Wang, "Experimental evaluation of the tri-polarized MIMO channel properties based on a compact multimode antenna," *IEEE Access*, vol. 7, pp. 67807–67817, 2019.

[16] D. Piao, M. Wang, J. Zuo, L. Zhang, and Y. Wang, "Compact and low-coupled tripolarized microstrip MIMO antenna based on parasitic patch loading," *IEEE Trans. Antennas Propag.*, vol. 69, no. 9, pp. 5992–5997, Sep. 2021.

[17] Y. Wang, D. Piao, and J. Song, "Implementation and MIMO performance assessment of two quad-polarized antennas," *IEEE Antennas Wireless Propag. Lett.*, vol. 21, pp. 2332–2336, 2022.

[18] L. Zou and C. Fumeaux, "A cross-shaped dielectric resonator antenna for multifunction and polarization diversity applications," *IEEE Antennas Wireless Propag. Lett.*, vol. 10, pp. 742–745, 2011.

[19] B. N. Getu and R. Janaswamy, "The effect of mutual coupling on the capacity of the MIMO cube," *IEEE Antennas Wireless Propag. Lett.*, vol. 4, pp. 240–244, 2005.

[20] M. R. Andrews, P. P. Mitra, and R. deCarvalho, "Tripling the capacity of wireless communications using electromagnetic polarization," *Nature*, vol. 409, no. 6818, pp. 316–318, Jan. 2001.

[21] C.-Y. Chiu, J.-B. Yan, and R. D. Murch, "Compact three-port orthogonally polarized MIMO antennas," *IEEE Antennas Wireless Propag. Lett.*, vol. 6, pp. 619–622, 2007.

[22] K. Park, J. Joung, S. Lim, and H. L. Lee, "A compact crossed inverted-V antenna with a common reflector for polarization diversity in the IoT," *Electronics*, vol. 8, no. 6, p. 637, Jun. 2019. [Online]. Available: https://www.mdpi.com/2079-9292/8/6/637

[23] G. P. Ramesh and A. Rajan, "Microstrip antenna designs for RF energy harvesting," in *Proc. Int. Conf. Commun. Signal Process.*, Apr. 2014, pp. 1653–1657.

[24] A. Rajawat, K. M. Agrawal, and P. K. Singhal, "Design, implementation and analysis of wide-band antenna with novel DGS for RF energy harvesting," *Mater. Today, Proc.*, Mar. 2023. [Online]. Available: https://www.sciencedirect.com/science/article/pii/S2214785323015067

[25] B. R. Behera, S. K. Mishra, M. H. Alsharif, and A. Jahid, "Reconfigurable antennas for RF energy harvesting application: Current trends, challenges, and solutions from design perspective," *Electronics*, vol. 12, no. 12, p. 2723, Jun. 2023. [Online]. Available: https://www.mdpi.com/2079-9292/12/12/2723

[26] G. Thiele and E. Ekelman, "Design formulas for vee dipoles," *IEEE Trans. Antennas Propag.*, vol. AP-28, no. 4, pp. 588–590, Jul. 1980.

[27] C. A. Balanis, *Antenna Theory: Analysis and Design*. Hoboken, NJ, USA: Wiley, 2005.

[28] Simulia. (2023). *CST Studio Suite*. [Online]. Available: https://www.3ds.com/

[29] S. J. Orfanidis. (2016). *Electromagnetic Waves and Antennas*. [Online]. Available: https://www.ece.rutgers.edu/~orfanidi/ewa/

[30] P. Meyer and D. S. Prinsloo, "Generalized multimode scattering parameter and antenna far-field conversions," *IEEE Trans. Antennas Propag.*, vol. 63, no. 11, pp. 4818–4826, Nov. 2015.

[31] C. Clarke, "The turnstile," *Feminist Stud.*, vol. 18, no. 3, p. 626, 1992.

[32] *Hack RF One: Great Scott Gadgets*. Accessed: Aug. 10, 2023. [Online]. Available: https://greatscottgadgets.com/hackrf/

[33] *USRP N210: Ettus Research*. Accessed: Aug. 10, 2023. [Online]. Available: https://www.ettus.com/all-products/un210-kit/

Dimitrios G. Arnaoutoglou was born in Thessaloniki, Greece, in September 1998. He received the B.S. degree in electrical and computer engineering from the Democritus University of Thrace, Komotini, Greece, in 2021. He is currently pursuing the Ph.D. degree in electrical engineering with the Democritus University of Thrace, Xanthi, Greece.

His research interests include multiferroics devices, and microwave systems for space applications and biomedical microwave applications.

Antigone-Aikaterini G. Kyriakou was born in Xanthi, Greece, in July 1997. She received the bachelor's degree from the Department of Electrical Engineering and Computer Science, Democritus University of Thrace, Xanthi, in 2020, and the M.Sc. degree (Hons.) in applied mathematics from the Democritus University of Thrace in 2023, where she is currently pursuing the Ph.D. degree.

She is a Teaching Assistant with the Democritus University of Thrace. Her main research interests include bioengineering, 3-D antenna designing and electromagnetic simulations, and pedagogy of the positive sciences.

Ms. Kyriakou received the Distinction from the 2018 IEEE International Symposium on Antennas and Propagation and USNC-URSI Radio Science Meeting of the IEEE Antennas and Propagation Society (APS) being a member of the DUTh Radiolocation Team, as a 2018 Design Contest Finalist.

Theodoros N. F. Kaifas (Senior Member, IEEE) received the B.Sc. degree in physics and the M.Sc. and Ph.D. degrees in electronic physics (radioelectrology) from the Department of Physics, School of Science, Aristotle University of Thessaloniki (AUTH), Thessaloniki, Greece, in 2004.

Since 1993, he has been a member of the Radio Communications Laboratory (RCL), Department of Physics, AUTH, where he has been an Adjunct Professor with the Program of Postgraduate Studies in Electronic Physics (Radioelectrology). From 2001 to 2008, he was an Adjunct Professor with the Department of Information and Electronic Engineering, International Hellenic University, Thermi, Greece. From 2006 to 2007, he was with the Department of Technology Management, University of Macedonia, Thessaloniki. He is currently an Assistant Professor with the Department of Electrical and Computer Engineering, Democritus University of Thrace (DUTH), Xanthi, Greece. He has a broad knowledge and experience in information technology and communications and an expertise in wireless communications, satellite communications, RF/microwave circuits, antenna analysis and design, and computational methods in electromagnetics accompanied by extensive contribution in relative literature and funded research projects.

Dr. Kaifas is a member of the ARIS Members Society, the Hellenic Physicist Union, the Hellenic Club of Electronic Physicists, and the Karatheodori Friends Association.

Georgios Ch. Sirakoulis (Senior Member, IEEE) received the Dipl.Eng. and Ph.D. degrees in electrical and computer engineering from the Democritus University of Thrace (DUTh), Komotini, Greece, in 1996 and 2001, respectively.

He is currently a Professor and the Head of the Department of Electrical and Computer Engineering at DUTH. He has published more than 340 technical articles. He is the co-editor of seven books, the coauthor of 32 book chapters, and the guest editor of 16 special issues. His research interests include future and emergent electronic devices, circuits, models, and architectures, unconventional computing, memristors, cellular automata, quantum cellular automata, bioinspired computation/biocomputation and bioengineering, and modeling and simulation.

Dr. Sirakoulis is in TCs of IEEE CASS, such as TC Cellular Nanoelectronics and Gigascale Systems (Nano-Giga) (as the Chair), TC IEEE Cellular Nanoscale Networks and Array Computing Technical Committee (CNAAC) (as the Secretary), the IEEE Nanotechnology Council, the VP-Publications Chair of IEEE NTC since 2024, the NTC Technical Committee on Nanoelectronics, the Vice Chair of IEEE Task Force on Unconventional Computing, and the IEEE Greece Section Treasurer. He is an Editor of IEEE TRANSACTIONS ON NANOTECHNOLOGY, *IEEE Nanotechnology Magazine*, *Microelectronics Journal*, *Integration, the VLSI Journal*, and the *Journal of Cellular Automata*.

George A. Kyriacou (Senior Member, IEEE) was born in Famagusta, Cyprus, in March 1959. He received the Diploma and Ph.D. degrees (Hons.) in electrical engineering from the Democritus University of Thrace, Xanthi, Greece, in 1984 and 1988, respectively.

Since January 1990, he has been with the Department of Electrical and Computer Engineering, Democritus University of Thrace, where he is currently a Professor and the Director of the Microwaves Laboratory and was the Director of Graduate Studies from 2005 to 2010. He has authored more than 250 journal articles and conference papers and supervised eight Ph.D. and 15 M.Sc. theses and more than 110 diploma theses. His main research interests include microwave engineering, open waveguides and antennas in anisotropic media, software-defined and cognitive radio, computational electromagnetics, and biomedical engineering.

Dr. Kyriacou is a member of the Technical Chamber of Greece and the European Microwave Association. He has been serving as an Associate Editor for *IET Microwaves, Antennas and Propagation* since 2015.